

# Windbreak Aerodynamics: Is Computational Fluid Dynamics Reliable?

P. Bourdin · John D. Wilson

Received: 6 February 2007 / Accepted: 29 August 2007 / Published online: 3 October 2007  
© Springer Science+Business Media B.V. 2007

**Abstract** To investigate the suitability of computational fluid dynamics (CFD) with regard to windbreak aerodynamics, simulations are performed with a state-of-the-art numerical scheme (Fluent) and compared against experimental data for two- and three-dimensional disturbances, namely the case of a long straight porous shelter fence and the case of a shelter fence erected in a square about an enclosed plot. A thorough sensitivity study quantifies the impact of numerical choices on the simulation (e.g. grid-point density, domain size, turbulence closure), and leads to guidelines that should ensure objective simulation of windbreak flows. On a fine grid Fluent's "realizable  $k-\epsilon$  closure" gives results that are in qualitative accord with the observed mean winds.

**Keywords** Numerical flow simulation · Shelter · Turbulent wind flow · Windbreak

## 1 Introduction

A long, straight windbreak represents one of the prototypical disturbances of the atmospheric surface layer, and as such is an interesting criterion for the performance of micrometeorological models. Computations by [Wilson \(1985\)](#) and others since (e.g. [Wang and Takle 1995](#); [Packwood 2000](#)) using various conventional Reynolds-averaged Navier–Stokes (RANS) closures have shown convincingly that mean wind reduction is quite well calculated, with weak sensitivity to the choice of turbulence closure, in neutral, perpendicular winds. As emphasized by [Wilson \(2004b\)](#) inevitably there is a spread of these solutions (relative to observations) reflecting not only the choice of closure, but also differing numerical details, such as domain size, resolution, etc. However what is more disconcerting is that simulations by

---

P. Bourdin (✉)

Department of Aerospace Engineering, University of Bristol, Bristol BS8 1TR, UK  
e-mail: patrick.bourdin@gmail.com

J. D. Wilson

Department of Earth and Atmospheric Sciences, University of Alberta, Edmonton, AB, Canada T6G 2E3  
e-mail: jaydee.uu@ualberta.ca

Wilson (2004b) of the influence of angle of approach (“obliquity”) to a single shelter fence agreed poorly with corresponding observations of mean winds, while simulations by Wilson and Yee (2003) of neutrally-stratified flows at normal incidence to an array of parallel wind-breaks were wholly unsatisfactory. This raises the question of whether the RANS approach may be inadequate to describe disturbed surface-layer flows in their generality?

The aim of the study is to examine this question, and stated more broadly, to assess the potential of computational fluid dynamics (CFD) for accurately and objectively (no parameter ‘tuning’) representing disturbed micrometeorological flows. This will be done by comparing simulations of the challenging case of a square shelterbelt surrounding an enclosed plot against the observations of Wilson and Flesch (2003). However before progressing to that level of complexity we study the simpler case (long straight fence) in order to systematically determine what is the necessary domain size and resolution, to ensure solutions are grid-independent. Section 2 describes the computational tools here used to predict two- and three-dimensional turbulent flows through porous barriers. We chose the general-purpose proprietary CFD software Fluent 5.5 from Fluent Inc., for it is an undisputed, well-known, standard flow solver in the engineering world. Sections 3 and 4 report and discuss comparisons between wind measurements and numerical flow predictions about a long, straight, porous fence standing perpendicular to the free stream (Bradley and Mulhearn 1983; Wilson 2004a), and a square, porous fence exposed to normal and oblique flows (Wilson and Flesch 2003). For all the computations, a neutrally-stratified atmospheric surface layer has been assumed (i.e. no buoyancy effects). Then, under the Boussinesq approximation, the governing equations required to be solved are the Reynolds equations for an incompressible fluid free from any body force.

## 2 Computational Set-up

### 2.1 Flow Solver

Fluent uses a cell-centred, segregated approach for solving, on a collocated, unstructured grid, the discretized RANS equations resulting from the application of the finite-volume method. Segregated implies here that the code sequentially solves the momentum, then continuity (recast as a pressure-correction equation), and then turbulence equations. To handle non-linearity in the equations, and to account for the natural coupling existing between the governing equations, several iterations of this solution loop, based on the SIMPLE family of algorithms (Patankar 1980), must be performed before a converged solution is obtained. More details about the solver are given in Appendix A. Unless otherwise stated, all the computations have been carried out using a second-order accurate central discretization for the diffusion terms, a second-order accurate upwind discretization for the advection terms and, where relevant, a second-order accurate time discretization. Among the SIMPLE family of algorithms, we selected the SIMPLER revision of van Doormaal and Raithby (1984) to enable the pressure-velocity coupling.

### 2.2 Pre-processing

Grids were generated by using straight, graded edges. The stretching ratio between two adjacent spacings along these edges was kept within the range 0.8–1.2. For the two-dimensional (2D) studies, only rectangular grids were used. For the three-dimensional (3D) studies, in order to moderate the number of computational cells and hence enhance computing effi-

ciency, the combination of a rectangular grid (in the near field) and a skewed grid (in the far field) was used. Further details will be given in Sects. 3 and 4.

### 2.3 Turbulence modelling

Because of the Reynolds averaging procedure, the governing equations exhibit additional unknown variables, the so-called Reynolds stresses, that need to be parameterized for the equation system to be closed and then solved. The closures (turbulence models) we used are briefly reviewed in the following two sub-sections.

#### 2.3.1 $k$ - $\epsilon$ models

These are two-equation eddy-viscosity models: Reynolds stresses are linearly related to the mean-velocity gradients (Boussinesq hypothesis) through an eddy viscosity coefficient,  $\mu_t$ . Two additional transport equations must then be solved (one for  $k$ , the turbulent kinetic energy—hereafter TKE—and another one for the TKE dissipation rate,  $\epsilon$ ) to compute the local values of the eddy viscosity, assumed to be equal to  $C_\mu k^2/\epsilon$ . The variants available within Fluent are the following:

- standard  $k$ - $\epsilon$  model (Launder and Spalding 1972);
- renormalization-group (RNG)  $k$ - $\epsilon$  model (Yakhot and Orszag 1986);
- realizable  $k$ - $\epsilon$  model (Shih et al. 1995).

Note that the term ‘realizable’ in the latest model means the modelled Reynolds stresses satisfy certain mathematical constraints consistent with the physics of turbulent flows, namely positivity of the normal Reynolds stresses and satisfaction of the Schwarz inequality by the tangential Reynolds stresses ( $\overline{u'_i u'_j} \leq \overline{u'^2_i} \overline{u'^2_j}$ ,  $i \neq j$ ). Neither the standard  $k$ - $\epsilon$  model nor the RNG  $k$ - $\epsilon$  model is guaranteed to produce physically-consistent turbulent stress tensors at every grid point. The major differences among the three models lie, (1) in the specification of the generation and destruction terms in the  $\epsilon$  equation, (2) in the ratios of the diffusivities of  $k$  and  $\epsilon$  to the eddy viscosity, and (3) in the method of computing the eddy viscosity ( $C_\mu$  is a constant within the standard and RNG models, whereas it is made variable within the realizable model by sensitizing it to the mean rate-of-strain tensor and the transported turbulence quantities  $k$  and  $\epsilon$ ).

#### 2.3.2 Reynolds stress models (RSM)

With RSM, second-order closure of the RANS equations is obtained by solving differential transport equations for each Reynolds stress  $\overline{u'_i u'_j}$ , whose gradients appear in the mean momentum equations. The Reynolds stress transport equations, derived from the exact (instantaneous) momentum equations, introduce in turn new terms that need to be modelled, namely the turbulent diffusion of  $\overline{u'_i u'_j}$ , its dissipation rate  $\epsilon_{ij}$ , and the so-called pressure-strain term  $p'(\partial u'_i/\partial x_j + \partial u'_j/\partial x_i)$ . In Fluent, the turbulent diffusion term is always modelled through a gradient-diffusion law (Lien and Leschziner 1994). Regarding the dissipation term, it is assumed that the scales of motion responsible for it are isotropic, so that  $\epsilon_{ij} = \frac{2}{3}\delta_{ij}\epsilon$ , where  $\delta_{ij}$  is the Kronecker index. Concerning the pressure-strain term, it is modelled either linearly (Launder 1989) or quadratically (Speziale et al. 1991) with respect to the Reynolds stresses. Note that, unlike the quadratic pressure-strain model, the linear pressure-strain model requires a correction to account for the ‘wall reflection effects’ in order to obtain a

satisfactory solution in the logarithmic region of a neutral turbulent layer. In Fluent, this correction is optional; we tested the linear pressure–strain model with and without this correction term.

### 2.4 Boundary treatment

At the computational domain inflow (upstream and top<sup>1</sup> boundaries) Reynolds-averaged velocity components and transported turbulence quantities (i.e.  $k$ ,  $\epsilon$ , or  $\overline{u'_i u'_j}$ ) are specified as follows, assuming a neutrally stratified turbulent atmospheric surface layer in local equilibrium:

$$\bar{u} = \frac{u_{*\infty} \cos \beta}{\kappa} \ln \frac{z}{z_0}, \tag{1}$$

$$\bar{v} = \frac{u_{*\infty} \sin \beta}{\kappa} \ln \frac{z}{z_0}, \tag{2}$$

$$\bar{w} = 0, \tag{3}$$

$$k = C_{\mu_{std}}^{-1/2} u_{*\infty}^2, \tag{4}$$

$$\epsilon = \frac{u_{*\infty}^3}{\kappa z}, \tag{5}$$

where  $\kappa$  is the von Karman constant (in Fluent, by default  $\kappa = 0.4187$ ),  $\bar{u}$ ,  $\bar{v}$ , and  $\bar{w}$  are the Reynolds-averaged  $x$ -,  $y$ - and  $z$ -velocity components (the  $z$  axis being vertical),  $\beta$  is the obliquity angle of the (approaching) mean flow relative to the normal of the fence,  $u_{*\infty}$  is the friction velocity far upstream from the fence ( $u_{*\infty} = 0.4 \text{ m s}^{-1}$  in our computations),  $z_0$  is the roughness length, and  $C_{\mu_{std}}$  is the constant arising in the definition of the turbulent viscosity in the standard  $k$ – $\epsilon$  model ( $C_{\mu_{std}} = 0.09$ , hence the equilibrium TKE is  $k/u_{*\infty}^2 = 3.33$ , somewhat lower than typical field values, but not sufficiently so to be of concern). The RSM models have been used only during the 2D flow simulations (the plane of the flow being  $Oxz$ ), with the following equilibrium inlet conditions for the velocity variances and covariance:

$$\overline{u'^2} = 1.098k, \tag{6}$$

$$\overline{v'^2} = 0.655k, \tag{7}$$

$$\overline{w'^2} = 0.247k, \tag{8}$$

$$\overline{u'w'} = -0.255k. \tag{9}$$

At the computational domain outflow, flow field variables are extrapolated from the adjacent interior cells assuming the normal gradient vanishes and then an overall mass balance correction is performed. The porous windbreak itself is treated as a pressure discontinuity surface by applying the following pressure jump condition:

$$P_W - P_L = \frac{\rho(\vec{q} \cdot \vec{n})^2}{2} K_r, \tag{10}$$

where  $P_W$  ( $P_L$ ) is the Reynolds-averaged pressure in the windward (leeward) cell,  $\vec{q}$  is the mean flow velocity vector at the interface of those two cells,  $\vec{n}$  is the unit vector normal

<sup>1</sup> The simplest appropriate upper boundary condition for this disturbed surface-layer flow would prescribe a fixed vertical momentum flux (i.e. driving shear stress  $-u_{*\infty}^2$ ) and a vanishing mass flux ( $W = 0$ ). However we were unable to configure Fluent this way, and prescribed instead a ‘velocity inlet boundary condition’, which required that the upper boundary be very slightly sloped, lying slightly higher above ground at the downwind boundary than at the upwind boundary.

to the cell face and  $K_r$  is the pressure drop coefficient (also termed resistance coefficient) of the windbreak.<sup>2</sup> While the formalism is slightly different, this treatment is numerically equivalent to the common practice of imposing a distributed momentum sink at the location of the barrier.

A no-slip condition is enforced at the ground, where the shear stress (required to compute the right-hand side (RHS) of the discretized momentum equations) is extrapolated from the prescribed surface roughness length and the mean-flow velocity at the centroid of the ground-adjacent cell (hereafter denoted point  $p$ ) by assuming a shallow neutral turbulent layer in equilibrium:

$$U_p = \frac{(\tau_0/\rho)}{\kappa C_\mu^{1/4} k_p^{1/2}} \ln \frac{z_p}{z_0}. \quad (11)$$

Here  $U_p$ ,  $\tau_0$ ,  $k_p$  and  $z_p$  are respectively the mean-flow velocity along the wall at point  $p$ , the shear stress on the wall in the direction of the velocity  $U_p$ , the TKE at point  $p$ , and the distance of point  $p$  from the wall.

Still resorting to the local equilibrium hypothesis, the turbulent quantities at the ground-adjacent cells are computed as follows:

- the  $k$  equation is solved at the ground-adjacent cells by using  $\partial k/\partial n = 0$  at the ground, and setting the production of  $k$  to  $P_k \simeq \tau_0 \partial U/\partial z = \tau_0^2/(\kappa \rho C_\mu^{1/4} k_p^{1/2} z_p)$  and its dissipation rate to  $\epsilon = u_{*\infty}^3/(\kappa z_p)$  at the centroid of the ground-adjacent cells;
- the  $\epsilon$  equation is not solved at the ground-adjacent cells, but is computed using the previous relation instead;
- the Reynolds stresses are computed from relations 6 to 9.

## 2.5 Convergence criteria

All the computations were continued until the global mass imbalance became smaller than 0.1% of the inlet mass flow rate and until the global specific difference between the RHS and the left-hand side (LHS) of the discretized momentum and turbulence equations became smaller than 0.1% (i.e.  $\sum |RHS - LHS|/\sum |RHS| < 0.001$ ). The drag on the ground was also monitored during the iterative numerical procedure to confirm convergence, and as a final check the local residuals (i.e. the mass imbalance and the specific RHS-to-LHS differences of the momentum and turbulence equations within each cell) were screened to make sure they were indeed small everywhere in the computational domain compared to a prescribed tolerance. For the local momentum and turbulence equation residuals, the tolerance was set to 0.1%. Concerning the local mass imbalance, the tolerance was set to  $0.0001 \text{ kg s}^{-1}$ , which corresponds to one-hundredth of the smallest mass flow rate one could expect through a cell face in the computational domain. In practice, we pushed the convergence beyond those limits so that the global and local residuals always levelled out at values much smaller (by at least two orders of magnitude) than their prescribed ‘safe’ limits.

## 3 Results for the Case of a Long, Straight Fence

This section assesses the ability of Fluent concerning the simulation of 2D wind flows through porous fences in the atmospheric surface layer. To this end, we compared RANS-predicted

<sup>2</sup> Note that in this paper, the definition of the resistance coefficient differs by a factor of 2 from that of Wilson (1985, 2004b). Both conventions are in widespread use.

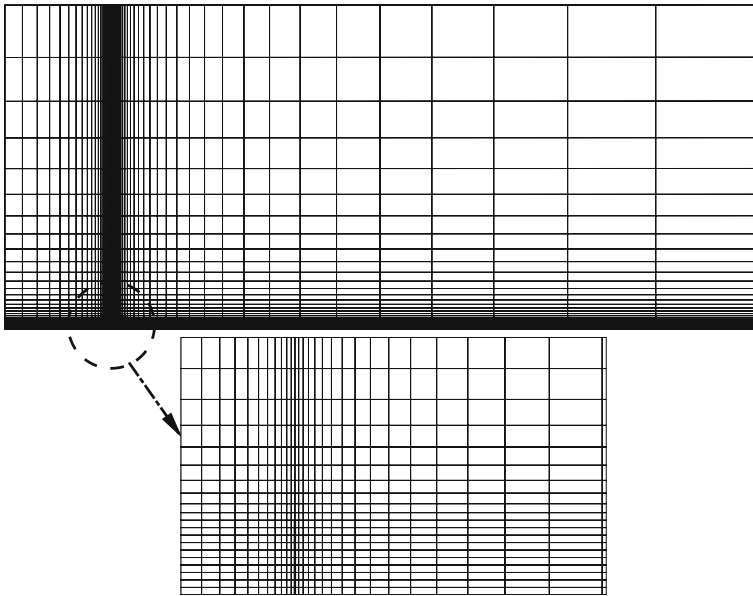


**Fig. 1** Global view of the computational grid and details around the fence.  $[-21 : 125; 62]_{25,35}^{10,27}$ ,  $R_x = R_z = 1.2$ ,  $\Delta x_0 = h/20$

speed  $\sqrt{\overline{u}^2 + \overline{v}^2}$  with measured mean cup wind speeds (see Appendix B for justification). Given that the length-to-height ratio of the fence was large in the field experiments, and the approach flow was perpendicular to the fence (in the mean), the time-averaged measured flow fields can be legitimately compared to two-dimensional RANS numerical results (where translational symmetry is assumed along the fence length for the mean fields). For convenience, the computational domains used during the simulations will be denoted:  $[X_U/h : X_D/h, Z_T/h]_{N_{X_U}, N_{X_D}}^{N_{Z_F}, N_{Z_{AF}}}$  where  $h$  is the height of the fence,  $X_U =$  upstream-boundary abscissa (relative to the fence),  $X_D =$  downstream-boundary abscissa (relative to the fence),  $Z_T =$  top-boundary altitude,  $N_{X_U} =$  number of computational-cell columns upwind,  $N_{X_D} =$  number of computational-cell columns downwind,  $N_{Z_F} =$  number of computational-cell rows between the ground and the top of the fence (uniform vertical spacing),  $N_{Z_{AF}} =$  number of computational-cell rows above the fence. Also let  $R_x, R_z$  and  $\Delta x_0$  denote the stretching ratio in the  $x$ -direction (from the fence to the outer boundary;  $R_x = \Delta x^{n+1}/\Delta x^n$ , where  $n, n+1$  label the widths of consecutively more distant cells), the stretching ratio in the  $z$ -direction (from the fence top to the top boundary), and the horizontal spacing of the fence-adjacent cells respectively. A typical grid used during our simulations is shown in Fig. 1.

### 3.1 Bradley–Mulhearn Windbreak

The **Bradley and Mulhearn (1983)** experiment used a windbreak made of vertical slats of wood ( $1.2\text{ m} \times 0.08\text{ m} \times 0.01\text{ m}$ ) woven in a sheep netting of mesh  $0.15\text{ m} \times 0.15\text{ m}$ . This 50% porous fence was erected on a uniform plain whose measured roughness length  $z_0$  was  $0.002\text{ m}$ . Only the data corresponding to neutral atmospheric conditions were considered. The resistance coefficient characterizing the pressure drop across the fence was  $K_r = 3.94 \pm 0.03$  (from wind-tunnel tests reported by **Wilson (1985)**, allowing for the difference in notation

and taking the standard error as uncertainty measure). Unless stated otherwise, the numerical simulations reported in the remainder of this section used  $K_r = 4$  and  $z_0 = 0.002$  m.

### 3.1.1 Comparison with Earlier Numerical Studies

Wilson (1985, 2004b) used the Bradley–Mulhearn experiment as a test-case for his staggered RANS solver, which was based on a finite volume discretization and used the SIMPLEC algorithm. Potential contributions to the differences between Wilson’s simulations and the Fluent simulations to be shown below stem from these distinctions between the two numerical methodologies and/or their implementation:

1. Fluent uses a collocated grid for the pressure, momentum and turbulence fields, whereas Wilson used a staggered grid.
2. Unless otherwise stated, the Fluent simulations used a second-order upwind interpolation scheme for the advection terms, whereas Wilson used a power-law scheme.
3. Except where stated, the domain boundaries, the mesh spacings, and the turbulence closure for the Fluent simulations differed from those chosen by Wilson.

Here we need to note that, although Wilson (1985) argued for the existence of a turbulent kinetic energy sink at the windbreak,<sup>3</sup> only where his focus was explicitly TKE (his Fig. 4) did he include it. Thus no distinction need be made in this respect between the 1985 simulations and the present treatment by Fluent, which, by virtue of the fact that the immersed elements are excluded from the control volumes,<sup>4</sup> invoked no TKE sink.

To the extent that it was within our power to do so, we sought to eliminate or minimize distinctions between the Fluent simulations and those of Wilson (1985). Thus in reference to the above distinctions between the codes, we believe we have minimized contributions from numerical choices (placement of the domain boundaries; mesh spacing and skew; interpolation scheme for advection; turbulence closure). The resulting Fluent simulations were generally in good accord with those reported by Wilson (1985), and we show an example on Fig. 2. It is not possible to explain with any certainty the differences that remain.<sup>5</sup> Arguably it is redundant to try, however, for as some consideration will confirm (e.g. see Wilson 2004b), these differences in outcome are actually quite small, compared to the far wider envelope needed to contain the spread of simulations, when once we admit other (equally reasonable seeming) choices—of mesh, of closure, etc. In summary, then, we confirm that RANS simulations on a rather coarse grid reproduce the mean velocity field of the Bradley–Mulhearn

<sup>3</sup> One may view the presence of a complex surface (here, the porous windbreak) in the airstream as implying that the air space is multiply connected. Formally, spatially continuous flow variables can be recovered by defining them to be a local spatial average ( $\cdot$ ) over a length embracing the barrier (e.g. Lien et al. 2005 and references therein). The resulting local instantaneous velocities are governed by a *filtered* Navier–Stokes equation, and contain terms representing momentum loss to the solid surface. Upon applying a further averaging operation to yield the Reynolds equations, the momentum sink gives rise to terms in the stress budget equation, and so there is a logical basis for implementing a sink for turbulent kinetic energy at the barrier. The (simulated) mean velocity field is not greatly affected by inclusion (or otherwise) of the TKE sink.

<sup>4</sup> Here we do not mean to imply Fluent is fundamentally more rigorous in its treatment of the unresolved flow about the fence; treatment as a pressure discontinuity surface is just as arbitrary as Wilson’s earlier treatment, and no ‘packaging’ of the momentum sink can sidestep the fact that a complex unresolved flow near and through the pores is being treated at a superficial level.

<sup>5</sup> These residual differences on Fig. 2 (between various solutions on the same, low resolution grid) merely emphasize the non-negligible impact of arbitrary modelling choices, viz., co-located versus staggered grid, order of approximation for derivatives, etc. The “slow recovery” of the mean wind in Wilson’s simulation is not observed in the present (Fluent) simulation, just as it was not observed in those of Wang and Takle (1995). We cannot explain this, but do not consider it fruitful to dwell on the matter.

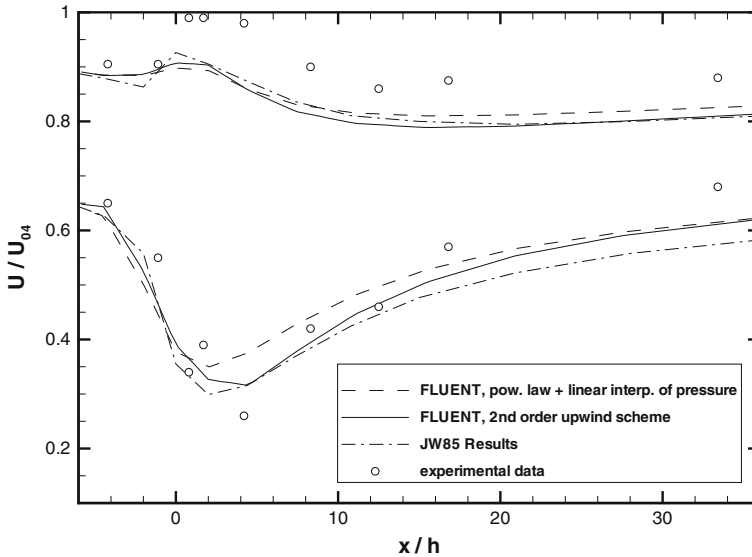


**Fig. 2** Observed and computed (2D RANS, standard  $k-\epsilon$  model) horizontal wind speeds upwind and downwind from the Bradley–Mulhearn windbreak (neutral stratification,  $h = 1.2$  m,  $z_0 = 0.002$  m,  $K_r = 4$ ). Lower curves correspond to  $z/h = 0.38$ , upper curves to  $z/h = 1.88$ . The horizontal wind speed,  $u$ , is normalized by  $u_{04}$ , the mean horizontal wind speed at  $z = 4$  m far upwind from the windbreak. The windbreak is located at  $x/h = 0$ . The same computational grid  $([-60 : 112; 47]_{10,13}^{4,20}, R_x = R_z = 1.2, \Delta x_0 = 2h)$  was used for all simulations, however Fluent relies on a collocated arrangement of variables at the cell centres of the grid, whereas Wilson’s method (JW85) relies on a staggered arrangement placing pressure at the cell centre, turbulent quantities at the vertices, and velocity components at the centre of each cell edge (curve ‘JW85 Results’ is the original simulation labelled “K- $\bar{e}$ - $\epsilon$ ” on Fig. 7 of JW85)

experiment quite well, just as earlier shown by Wilson (1985) and others subsequently (e.g. Wang and Takle 1995; Packwood 2000).

### 3.1.2 Sensitivity Studies

It goes without saying that the finer the computational mesh the smaller the truncation error (i.e. distinction between the discretization equations and the differential equations), and so the closer the numerical solution to the exact (but unknown) solution to the coupled RANS differential equations. However grid refinement does not *necessarily* procure a better agreement with observations. In the present case when resolution is refined to ensure grid independence<sup>6</sup> the resulting (Fluent,  $k-\epsilon$ ) simulation is superior (e.g. Fig. 3) to the low resolution simulation in terms of its accordance with the measured mean velocity field extremely close to the fence (and especially upwind). The high resolution Fluent  $k-\epsilon$  solution exhibits a narrower and deeper trough in relative wind speed than does the coarse grid solution, but the scatter (and wide streamwise spacing) of the available observations do not allow us to judge very definitely whether this represents an improved approximation to reality, or, on the contrary, a

<sup>6</sup> In the course of these comparisons of Fluent simulations with the Bradley–Mulhearn data, we carried out an exhaustive and systematic test of the impact of all aspects of the grid, viz. domain boundary placement and grid resolution. Space does not allow us to convey the details, but in summary, we can say that for the problem at hand, Fluent will provide grid-insensitive solutions so long as the following criteria are met:  $\Delta x_0 \leq h/5$ ;  $R_x, R_z \leq 1.2$ ;  $|X_U|, X_D \geq 21h$  and  $Z_T \geq 40h$ .

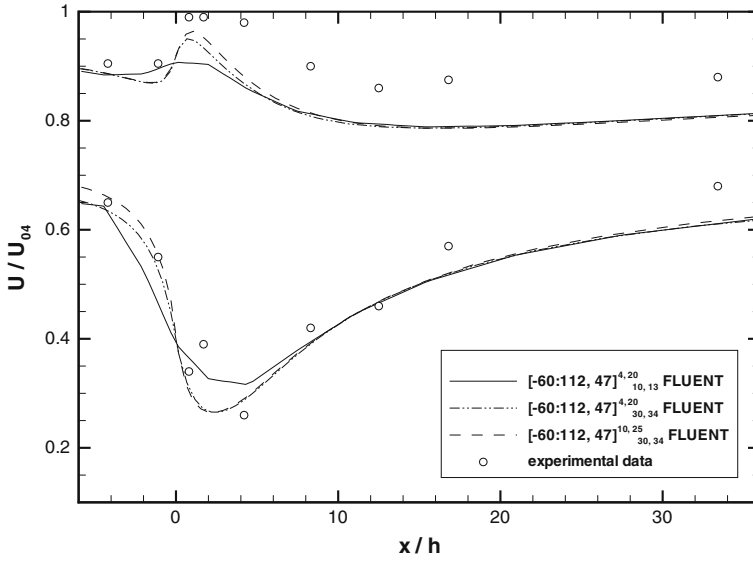


**Fig. 3** Effect of grid refinement on Fluent results (Bradley–Mulhearn case, standard  $k-\epsilon$  model, 2nd order upwind scheme,  $R_x = R_z = 1.2$ ). *Solid line* corresponds to the  $\Delta x_0 = 2h$  and  $N_{ZF} = 4$  case, *dashed double-dotted line* corresponds to the  $\Delta x_0 = h/20$  and  $N_{ZF} = 4$  case, and *dashed line* corresponds to the  $\Delta x_0 = h/20$  and  $N_{ZF} = 10$  case

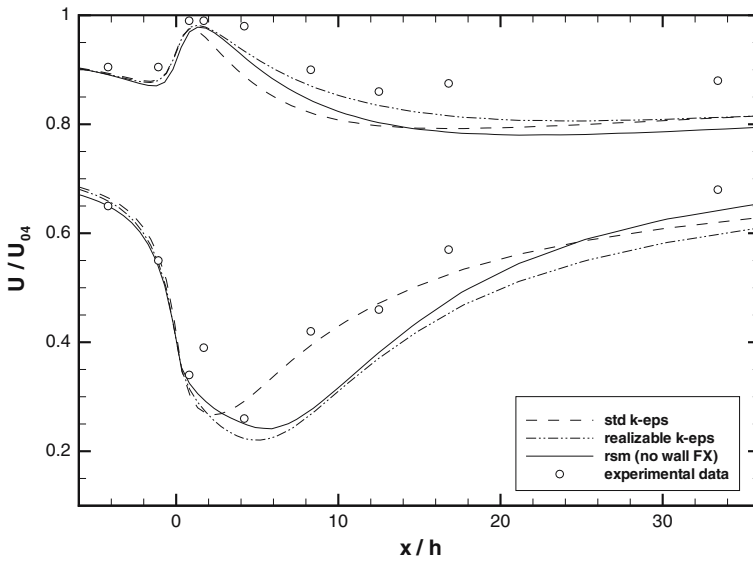


**Fig. 4** Observed and computed, normalized, horizontal wind speeds upwind and downwind from the Bradley–Mulhearn windbreak at  $z/h = 0.38, 1.88$ . Influence of turbulence modelling at fixed grid extent and density (grid  $[-21 : 125; 62]^{10,27}_{25,35}$ , with  $\Delta x_0 = h/20$  and  $R_x = R_z = 1.2$ )

degradation. *Probably* the latter is the case, if one adopts a mean square error criterion. Figure 4, which compares standard  $k-\epsilon$ , realizable  $k-\epsilon$ , and Reynolds-stress closures on the same refined grid, indicates that the more advanced (or at least, more complex) closures produce a deeper, broader relative wind speed trough than the standard  $k-\epsilon$  closure (consistent with Fig. 7 of Wilson 1985) and than actually observed. This is consistent, too, with outcomes reported by Wilson (2004b)—his Figs. 5, 6b—on the basis of simulations using exclusively second-order closures, viz. his finding that “the computed wind reduction curve is systematically deepened as computational resolution is improved, such that the low-resolution simulations of Wilson (1985) happily but fortuitously give best agreement with observations”.

It has been known for a long time that RANS simulations of TKE, whether from first-order or higher-order closure models, tend to be inferior to those of the mean velocity field. Fluent did not provide the option of invoking a TKE sink at the fence (as arguably would be necessary in a treatment of the flow domain as multiply-connected), but used a pressure jump condition instead, nevertheless, producing in all cases at least some signal of a ‘quiet zone’ in the near lee of the fence. Unsurprisingly there were large differences from closure to closure, and Fig. 5 demonstrates this. We do not have comprehensive observations at hand to judge which is the best of these computed patterns (and others not shown) of TKE.

### 3.2 Ellerslie Windbreak

The Ellerslie windbreak experiment (Wilson 2004a) involved a long, straight, porous, plastic fence of height  $h = 1.25$  m and length  $Y = 114$  m, exposed on a uniform plain of grass (roughness length  $z_0 \simeq 0.02$  m). Flow statistics were collected upwind and downwind from the fence at level  $z = h/2$ . The resistance coefficient of the fence, deduced from the pressure drop observed across a section of the material that had been mounted so as to block a uniform wind tunnel stream, was  $K_r = 4.8$ .

2D RANS simulations were carried out on grid  $[-21 : 40; 40]_{24,28}^{10,24}$ , with  $\Delta x_0 = h/20$ , and  $R_x = R_z = 1.2$ . Unless stated otherwise, the experimental values of  $K_r$  and  $z_0$  specified above were used. Numerical results were compared to experimental data corresponding to nearly normal incidence and nearly neutral stratification. Figure 6 shows the influence of turbulence modelling. The realizable  $k-\epsilon$  model is the most adequate two-equation model available in Fluent for reproducing the experimental data, giving the right streamwise location of the leeward wind speed minimum but overestimating the depth of the relative wind speed curve. Reducing  $K_r$  by a factor of 25% allowed the realizable  $k-\epsilon$  model to match the experimental data better, which was true also of simulations of the Bradley–Mulhearn experiment (not shown). Contrary to the Bradley–Mulhearn case, for the Ellerslie measurements the RSM approach featuring a linear pressure-strain model and no wall effects does not perform better than the realizable  $k-\epsilon$  model.

### 3.3 Conclusions from 2D Simulations

By performing parametric studies on the metrics of the computational domain, we observed that a state-of-the-art CFD method produces grid-independent results for the simulation of windbreak flows provided that the grid is sufficiently refined and that the outer boundaries are far enough from the barrier for the boundary conditions applied (velocity inlet and outflow) to be realistic and/or not to influence significantly the simulated flow around the windbreak. More quantitatively, the grid  $[-21 : 21; 40]_{25,25}^{10,24}$ ,  $\Delta x_0 = h/20$ ,  $R_x = R_z = 1.2$  suffices for Fluent to produce numerical results insensitive to further grid-density and/or grid-extent increases.

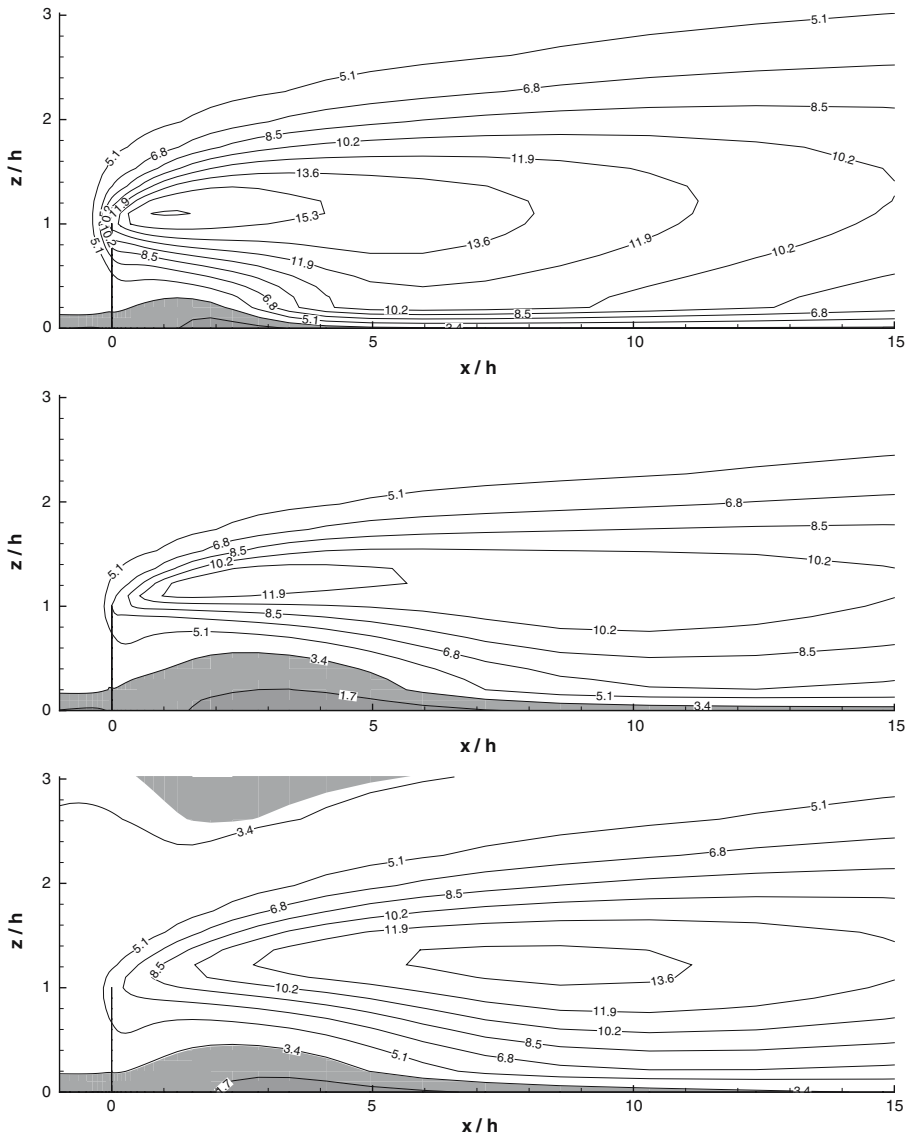


**Fig. 5** Normalized TKE contours ( $k/u_\infty^2$ ) from RANS simulations of the Bradley–Mulhearn windbreak (grid  $[-21 : 125; 62]_{25,35}^{10,27}$ , with  $\Delta x_0 = h/20$  and  $R_x = R_z = 1.2$ ). Top: standard  $k-\epsilon$  closure; middle: realizable  $k-\epsilon$  closure; bottom: RSM with linear pressure strain and no wall effect. The grey areas correspond to the so-called quiet zone for which the TKE is smaller than its approach, uniform value

By testing the numerous turbulence models available in the flow solver Fluent and comparing the resulting predictions to experimental data, it appeared that the realizable  $k-\epsilon$  model is the most reliable and objective (for our particular choice of boundary conditions at least—results may be different with a different set of boundary conditions). Performance of that model relative to the experimental data can be enhanced by lowering the resistance coefficient of the modelled fence relative to its true value (i.e. the ‘static’ value measured

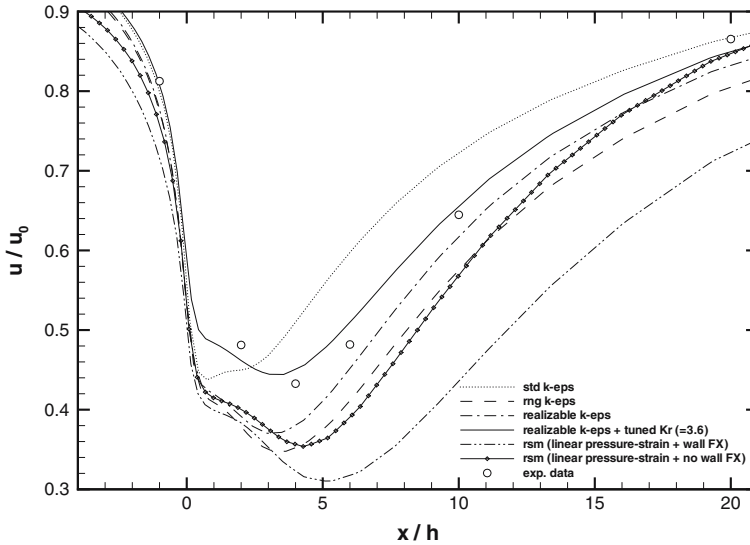


**Fig. 6** Observed and computed (2D RANS) horizontal wind speeds upwind and downwind from the Eilerslie windbreak (neutral stratification,  $h = 1.25$  m,  $z_0 = 0.02$  m,  $K_r = 4.8$ ) at  $z/h = 0.5$ . The horizontal wind speed,  $u$ , is normalized by  $u_0$ , the mean horizontal wind speed at  $z/h = 0.5$  far upwind from the windbreak. The windbreak is located at  $x/h = 0$

in an unshered laminar test flow). For the sake of objectivity we recommend against such unjustifiable ‘tuning’.

#### 4 Results for a Square Shelterbelt

The case modelled here corresponds to the experiment of [Wilson and Flesch \(2003\)](#): a square plot (sidelength  $D = 20$  m) sheltered on all four sides by a porous, plastic windbreak fence (height  $h = 1.25$  m, resistance coefficient  $K_r = 4.8$ ) is standing on uniform, level ground (roughness length  $z_0 = 0.015$  m).

The airflow disturbances within and around the plot are computed by using the RANS and URANS (Unsteady RANS) approaches. During their experiment, [Wilson and Flesch \(2003\)](#) found that the measured wind speeds (15-min averages from cup anemometers<sup>7</sup> were rather insensitive to the thermal stratification of the surface layer. Therefore, their data can reasonably be compared to our numerical results,<sup>8</sup> which assume neutral stratification.

<sup>7</sup> The experimental data for the square plot were taken directly from Figs. 11–14 of [Wilson and Flesch \(2003\)](#), i.e. the numbers that were cited (to one or two decimal places) at each of the instrument positions sampled. In turn, each such number was an eyeball best fit to the ensemble of available estimates as conveyed on Figs. 3–7 of that paper. The reader may track backwards to obtain a sense of the uncertainty in data cited here. Because of the uneven number of estimates across the instrument position-approach angle parameter space, a meaningful standard deviation or standard error cannot be given: the range is perhaps in this case an acceptable substitute. Let  $r = S/S_0$  designate the wind reduction ratio (or ‘normalized wind speed’). For a given location in the sheltered plot and for a given mean wind direction, we can express the range of observed values of  $r$  as  $\bar{r} \pm \epsilon$ , where  $\epsilon$  ranged from a minimum of about 0.03 through (most commonly) 0.05 to (at worst) 0.15. As a simple global estimate, the range might be expressed as  $\bar{r} (1 \pm 0.1)$ .

<sup>8</sup> We compared RANS-predicted speed  $\sqrt{\bar{u}^2 + \bar{v}^2}$  with measured mean cup wind speeds (see Appendix B for justification).

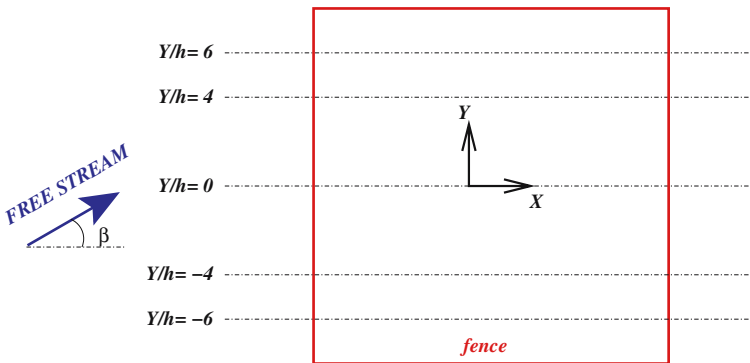


**Fig. 7** Nomenclature used in the square shelterbelt simulation

Let  $\beta$  denote the obliquity angle of the approach airflow (it is measured with respect to the normal vector of the windward face of the shelterbelt, see Fig. 7). Four types of approach airflow will be considered: normal flow (obliquity angle  $\beta = 0^\circ$ ); oblique flow with  $\beta = 15^\circ$ ; oblique flow with  $\beta = 30^\circ$ ; and corner flow (obliquity angle  $\beta = 45^\circ$ ).

#### 4.1 Gridding

Although we could have made use of symmetry with the RANS approach for the normal-flow and corner-flow cases and hence modelled only half the shelterbelt, we chose to design a single grid that would be suitable for all the obliquity angles and all the flow models.

Let  $x$ ,  $y$ ,  $z$  denote the axes of a Cartesian coordinate system, oriented as shown in Fig. 7, the  $z$ -axis being vertical and pointing upward. The origin is taken at the centre of the square plot (the square plot has then its corners located at  $(-8h; -8h)$ ,  $(-8h; 8h)$ ,  $(8h; -8h)$  and  $(8h; 8h)$  in the horizontal plane). The brick-shaped computational domain has its outer edges aligned with the  $x$ -,  $y$ -, and  $z$ -axes. Referring to our previous sensitivity studies on 2D grids, the length, width, and depth of the domain are chosen to be  $96h$ ,  $96h$ , and  $41h$  respectively, with  $-x_{\min} = x_{\max}(=48h)$  and  $-y_{\min} = y_{\max}(=48h)$ . The distance between one edge of the shelterbelt and the nearest outer boundary of the computational domain is then  $40h$ . The windbreak is uniformly discretized into 10 cells along its height and 80 cells along its sidelength. Anywhere else, the stretching ratio of the grid cells is 1.2 (from the interior towards the exterior of the domain). Views of the computational domain are shown in Fig. 8. Note that we used an O-topology to warp a Cartesian sub-domain whose faces are  $8h$  (i.e.  $D/2$ ) away from the nearest edge of the shelterbelt located inside. Compared to a stretched Cartesian grid, this peculiar topology allows us to save a substantial number of grid cells in the far field (which does not need to be as refined as the near-field mesh, because the flow field gradients are expected to be weak there). The total number of (hexahedral) cells is 454,272.

#### 4.2 RANS Results

All the computations were carried out using the experimental values of the resistance coefficient ( $K_r = 4.8$ ) and the roughness length ( $z_0 = 0.015$  m).

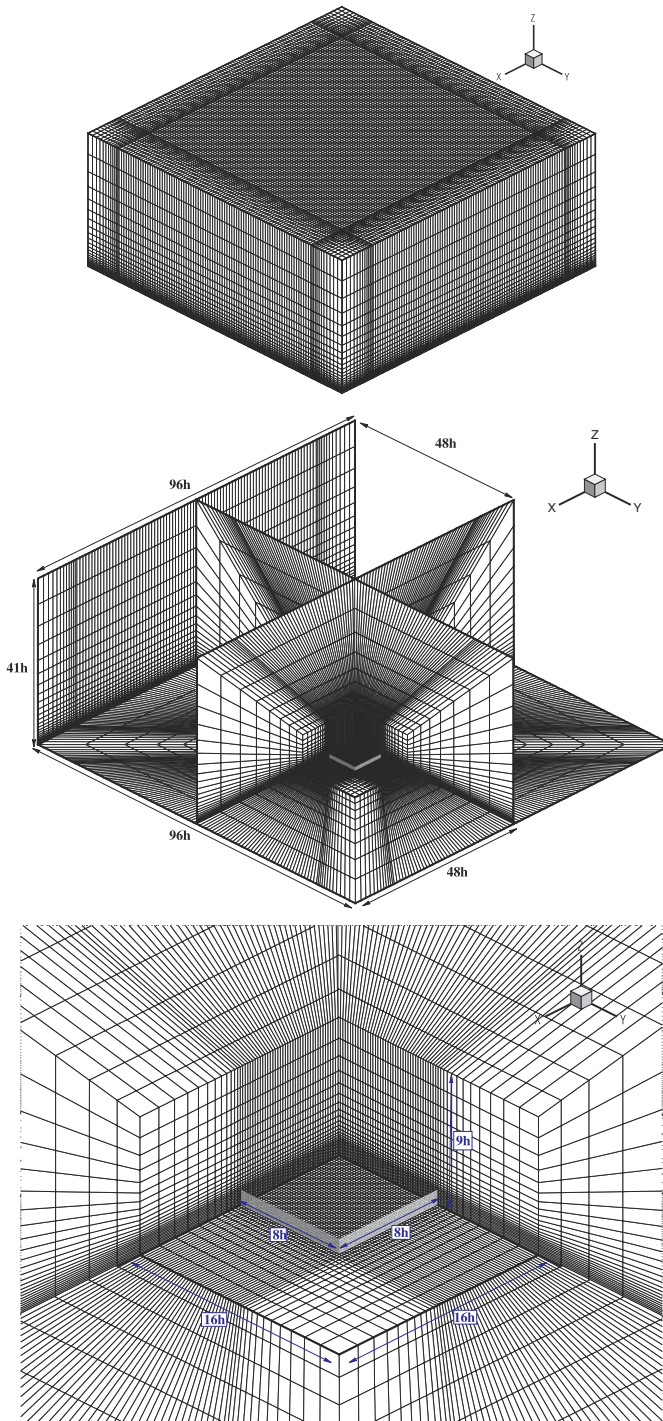


**Fig. 8** Isometric views of the computational domain; top: top and side boundaries, middle: cut-away view; bottom: details around one quarter of the shelterbelt

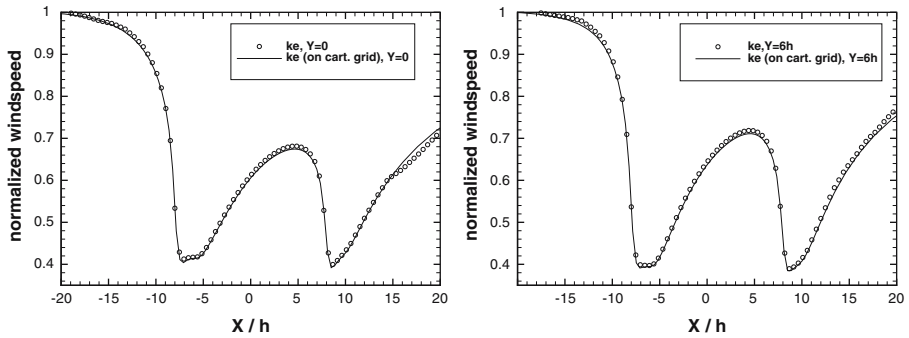


**Fig. 9** Normalized, horizontal wind speeds at  $z = h/2$  for the square shelterbelt ( $h = 1.25$  m,  $D = 20$  m,  $K_r = 4.8$ ,  $z_0 = 0.015$  m); RANS computations, standard  $k - \epsilon$  model; left:  $y = 0$ , right:  $y = 6h$ . The wind speed is normalized by its value far upstream at the same height level. Front fence is located at  $x/h = -8$ , rear fence is located at  $x/h = +8$ . Solid lines correspond to results on the stretched Cartesian grid, *circular symbols* correspond to results on the O-grid

#### 4.2.1 Assessment of the Grid

To ensure that the O-grid (Fig. 8) does not introduce or promote in the solution field any bias permitted by the selected numerical schemes, and that the solution is grid-independent, the normal-flow computation has been double-checked on a denser grid with an H-topology, the so-called stretched Cartesian grid. This ‘benchmark’ grid, strictly orthogonal, has a cell stretching ratio of 1 inside the square plot and of 1.2 outside (going from the windbreak towards the outer boundary of the computational domain). Symmetry is assumed through the  $xOz$  centre plane (RANS simulation, Normal Flow), so that only half the square plot is modelled. The characteristics of the stretched Cartesian grid are as follows: the sidelength and the height of the shelterbelt are uniformly discretized into 160 and 10 cells respectively; the depth is  $40h$  and the width (distance from the symmetry plane to the lateral outer boundary) is  $48h$ ; distance from the upstream boundary to the nearest side of the shelterbelt is  $20h$ ; distance from the downstream boundary to the nearest side of the shelterbelt is  $40h$ . In total the grid contains 735, 420 cells.

For these preliminary computations, the standard  $k - \epsilon$  closure was used. Comparison of the results in terms of wind speed transects at the transect level ( $z = h/2$ ) are shown in Fig. 9: one can note that the O-grid gives results as accurate as the Cartesian grid, despite being twice as coarse as the latter and featuring skewed computational cells.

#### 4.2.2 Choice of the Turbulence Closure and Comparison with the Experiment

During the 2D simulations, the best agreement with experiment was obtained with the realizable  $k - \epsilon$  closure. We chose to carry on with this closure for the 3D simulations. However, to make sure this model is still adequate in 3D flows, we compared against experimental data results obtained with this closure and results obtained with the standard  $k - \epsilon$  closure. This is shown in Fig. 10 in terms of horizontal-velocity transects at the transect-level ( $z = h/2$ ) for the normal flow case ( $\beta = 0^\circ$ ). One can see that along the centre line of the square plot ( $y = 0$ ), as well as along the  $y/h = 4$  line, the realizable  $k - \epsilon$  model gives results in good agreement with the experiment, whereas on balance the standard  $k - \epsilon$  closure is inferior, for it does not capture well the streamwise location and the magnitude of the wind speed minimum,

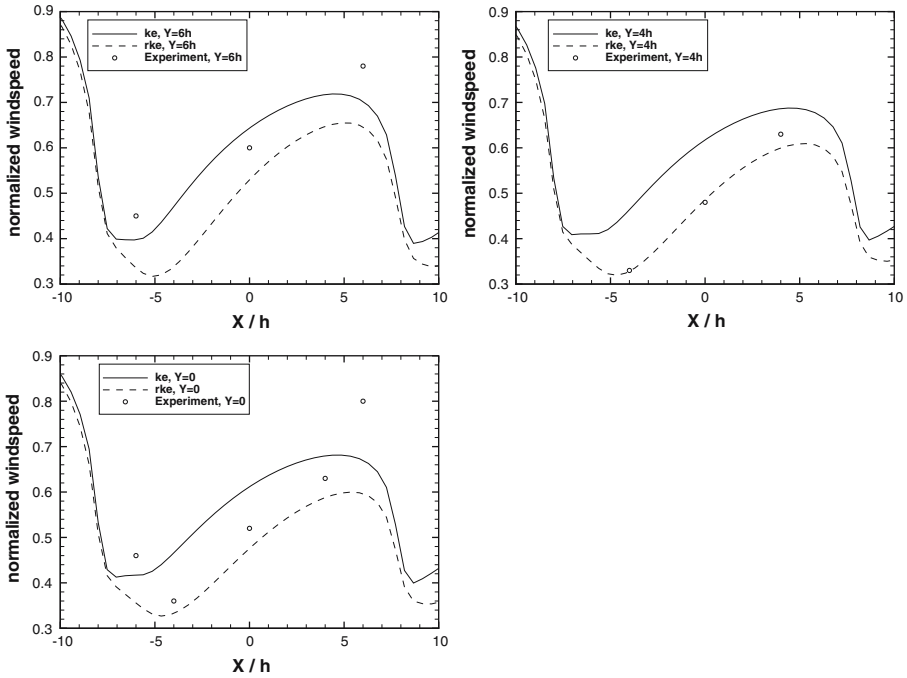


**Fig. 10** Observed and computed (RANS, standard and realizable  $k-\epsilon$  models) normalized, horizontal wind speeds at  $z = h/2$  for the square shelterbelt ( $h = 1.25$  m,  $D = 20$  m,  $K_r = 4.8$ ,  $z_0 = 0.015$  m);  $\beta = 0^\circ$ ; top left:  $y = 6h$ , top right:  $y = 4h$ , bottom:  $y = 0$ . The wind speed is normalized by its value far upstream at the same height level. Front fence is located at  $x/h = -8$ , rear fence is located at  $x/h = +8$

except in the case of the transect ( $y/h = 6$ ) near the downwind bounding fence. Note also that neither the standard nor the realizable models predict well the wind speed recovery near the downstream side of the shelterbelt (see point at  $x/h = 6$  for  $y = 0$ ). In summary, the realizable  $k-\epsilon$  model appears to be a safe choice to adequately mimic (at a low computational cost) the real flow, as was the case with the 2D configuration. This justifies our using the realizable  $k-\epsilon$  closure for the following RANS/URANS computations.

Figures 11–13 compare computed and measured transects of horizontal wind speed for obliquity angles varying from  $15^\circ$  to  $45^\circ$ . Once again, on balance, agreement between the realizable  $k-\epsilon$  simulation and the experiment is rather good except for a few locations in the plot, namely along ( $x = 0, y/h = -6$ ) for all obliquity angles, and along ( $x/h = 6, y = 0$ ) for the case  $\beta = 15^\circ$  (note: even these poorer model transects show some resemblance to the measured pattern, so are more faithful to reality than might have been anticipated in this difficult flow). In the corner flow case, there were sufficient experimental data along the diagonal of the plot to define a diagonal transect (from the windward corner to the leeward corner), see Fig. 14. Except in the immediate lee of the windward corner, the flow is quite well predicted along this streamwise diagonal.

### 4.2.3 Transect-level Fields

Contours of horizontal velocity at the transect level ( $z = h/2$ ) reveal the formation of a jet within the sheltered area when the obliquity angle increases (see Fig. 15). In the normal-flow

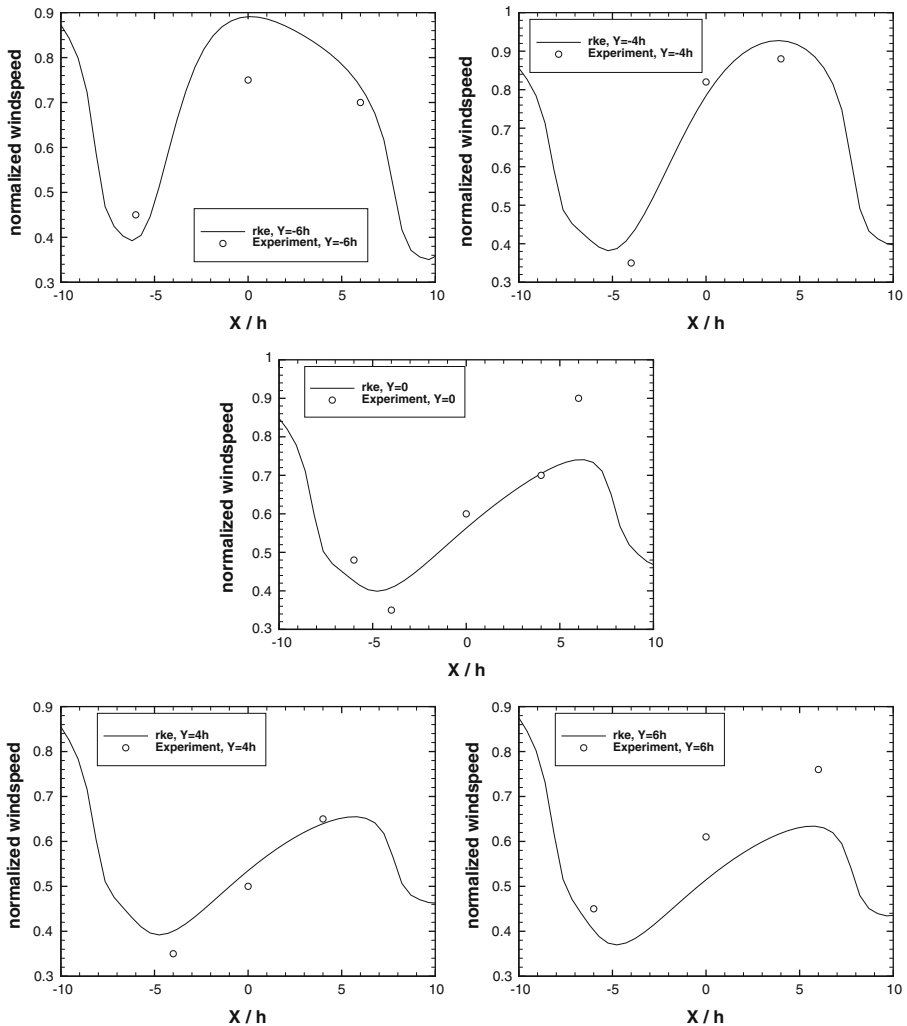


**Fig. 11** Observed and computed (RANS, realizable  $k-\epsilon$  model) normalized, horizontal wind speeds at  $z = h/2$  and  $y/h = \{-6, -4, 0, +4, +6\}$  for the square shelterbelt ( $h = 1.25$  m,  $D = 20$  m,  $K_r = 4.8$ ,  $z_0 = 0.015$  m);  $\beta = 15^\circ$ . The wind speed is normalized by its value far upstream at the same height level. Front fence is located at  $x/h = -8$ , rear fence is located at  $x/h = +8$

case, wind speed is reduced below 50% of its approach value, over the first half of the shelterbelt area. Over the second half the wind speed is about 60% of its approach value. Increasing the obliquity angle to  $15^\circ$  generates a pocket of slightly reduced wind speeds (representing 80–90% of the approach value) in the lee of the southern<sup>9</sup> side of the shelterbelt. At  $30^\circ$  and  $45^\circ$  obliquity angles, that pocket moves along the streamwise diagonal and the leeward corner of the shelterbelt, with wind speeds exceeding those in the open.

From the contours of TKE (Fig. 16), one can notice the presence of a ‘quiet zone’ (TKE smaller than the undisturbed value  $k/u_{*\infty}^2 = 3.33$ ) in the immediate lee of the windward

<sup>9</sup> The  $y$  axis is assumed to point north for the sake of the figure descriptions.

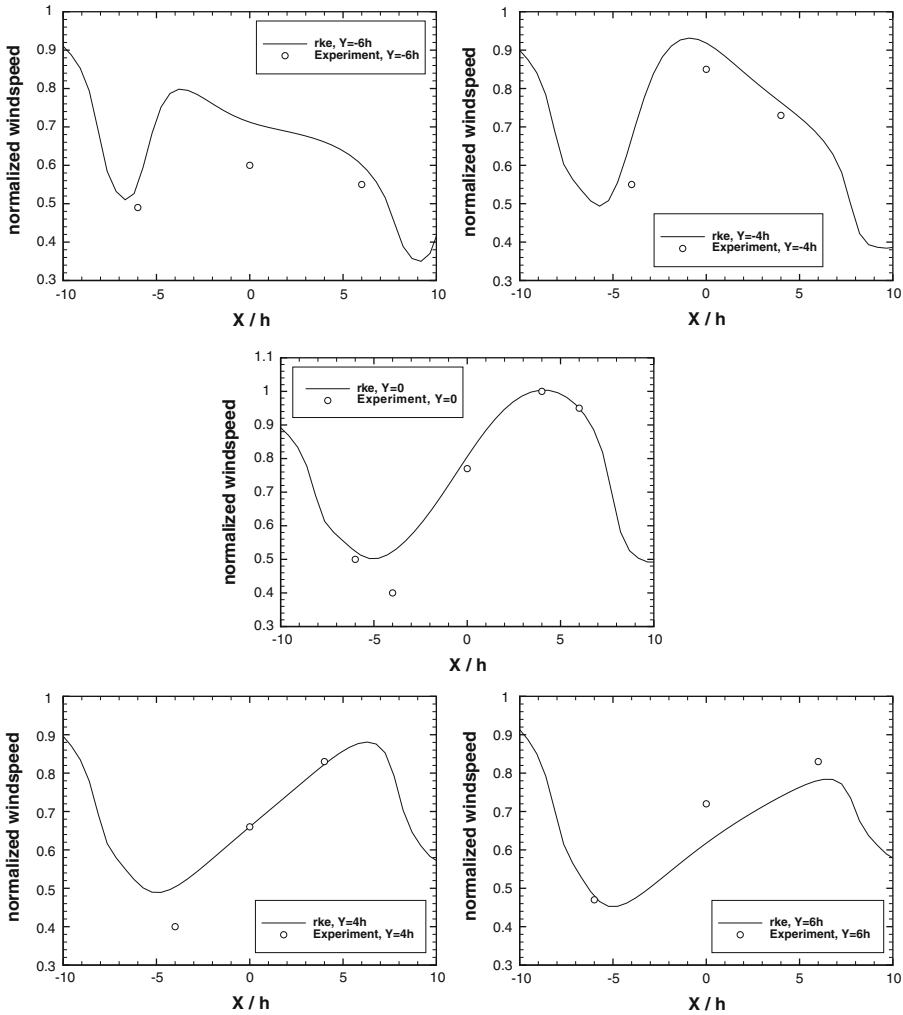


**Fig. 12** Observed and computed (RANS, realizable  $k-\epsilon$  model) normalized, horizontal wind speeds at  $z = h/2$  and  $y/h = \{-6, -4, 0, +4, +6\}$  for the square shelterbelt ( $h = 1.25$  m,  $D = 20$  m,  $K_r = 4.8$ ,  $z_0 = 0.015$  m);  $\beta = 30^\circ$ . The wind speed is normalized by its value far upstream at the same height level. Front fence is located at  $x/h = -8$ , rear fence is located at  $x/h = +8$

barrier(s). Note also the intrusion of a zone of increased TKE in the lee of the windward corner when the obliquity increases.

#### 4.2.4 Surface Pressure Fields

Relative pressure fields at level  $z/h = 0.1$  are shown in Fig. 17 for the normal-flow and corner-flow cases. In the normal-flow case, horizontal pressure gradients at that level are roughly steady in the first half of the square along the approach airflow direction, then they diminish in the second half and increase again in the last quarter, ahead of the leeward side

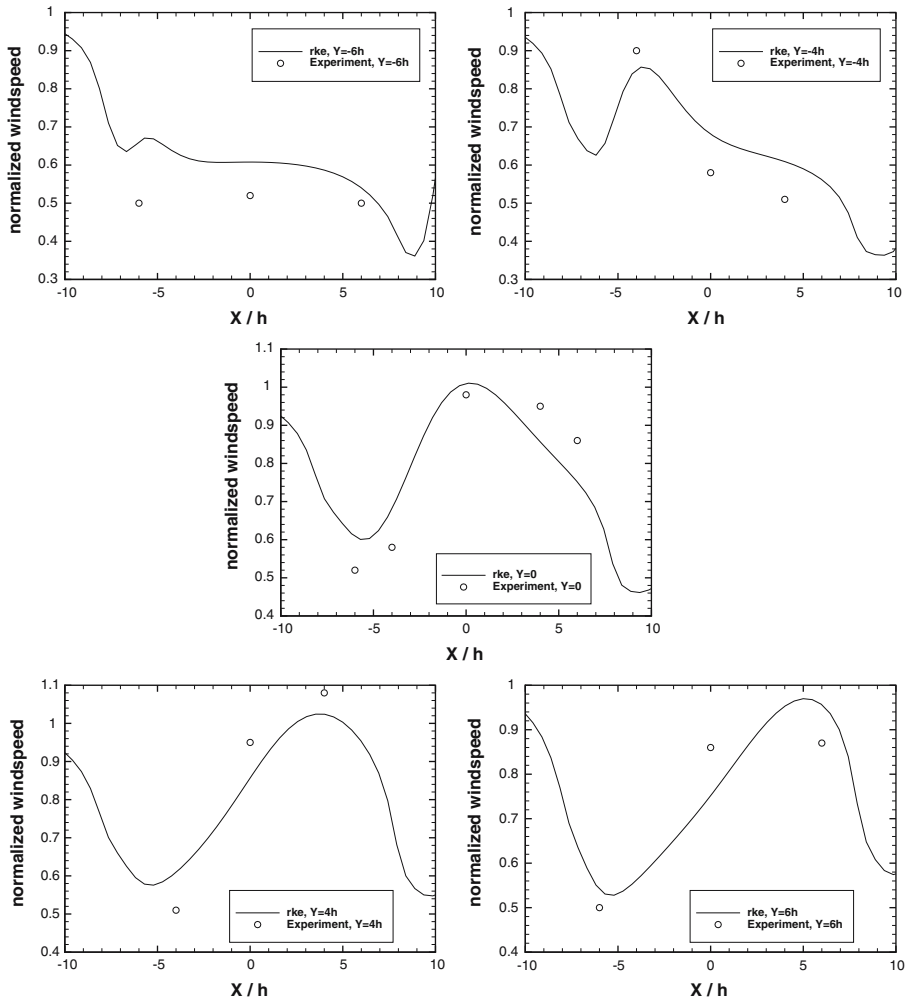


**Fig. 13** Observed and computed (RANS, realizable  $k-\epsilon$  model) normalized, horizontal wind speeds at  $z = h/2$  and  $y/h = \{-6, -4, 0, +4, +6\}$  for the square shelterbelt ( $h = 1.25$  m,  $D = 20$  m,  $K_r = 4.8$ ,  $z_0 = 0.015$  m);  $\beta = 45^\circ$ . The wind speed is normalized by its value far upstream at the same height level. Front fence is located at  $x/h = -8$ , rear fence is located at  $x/h = +8$

of the square. In contrast, in the corner-flow case, there is a pocket of stronger horizontal pressure gradients in the lee of the windward corner.

#### 4.2.5 Streamlines

Streamlines for the normal-flow and corner-flow cases have been re-constructed from the computed velocity fields. In the case of normal-flow the disturbance to streamlines is most marked near corners, away from which the flow appears ordered in the sense that a streakline emitted upstream at some height always remains above any other streakline emitted at the same station but at a lower height. In contrast the streamline pattern for the corner-flow case

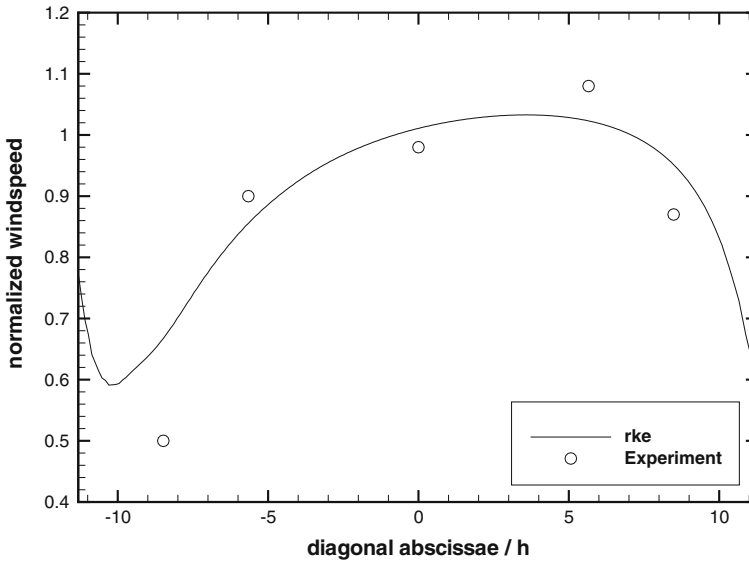


**Fig. 14** Observed and computed (RANS, realizable  $k-\epsilon$  model) normalized, horizontal wind speeds along the streamwise diagonal of the square plot at  $z = h/2$ ;  $\beta = 45^\circ$ . The wind speed is normalized by its value far upstream at the same height level. The diagonal abscissa ranges from the windward corner ( $-11.31h$ ) to the leeward corner ( $+11.31h$ )

(Fig. 18) is highly disturbed, with higher streamlines plunging into the sheltered volume and lower streamlines spreading crosswise, suggesting the presence of helicity (streamwise vorticity) in the flow.

#### 4.3 URANS Simulations

To check whether any unsteady phenomena might occur (e.g. vortex shedding), second-order accurate URANS simulations have been performed for the case  $\beta = 30^\circ$ . Resorting to dimensional analysis, with the shelterbelt sidelength as length scale  $L$  and the approach velocity at fence height as velocity scale  $U$ , the time scale of the mean flow should be of the order of  $L/U = 5$  s. A timestep 10 times smaller than this was chosen to carry out the computations (i.e.  $\Delta t = 0.5$  s). Transient simulations were initialized either by using the existing (steady) RANS solution, or by prescribing an equilibrium neutral atmospheric surface-layer flow over the entire computational domain. These two alternative initializations caused the transient simulations to converge towards the same steady state (see Fig. 19). Halving the timestep did not alter the numerical results, so we may assume our choice of timestep was satisfactory. The steady solution reached in the course of the URANS simulations has been compared to the solution obtained previously with the steady-flow RANS solver: as one can see from Fig. 20, steady states obtained from both approaches are the same, overlooking minor differences that make the URANS fields agree slightly better with the experimental data. We conclude that windbreak flow can legitimately be treated as steady state, in the sense that no gain in fidelity accrues from retaining the local tendency term in the Reynolds equations, ending speculation (Wilson 2004b) on that score.

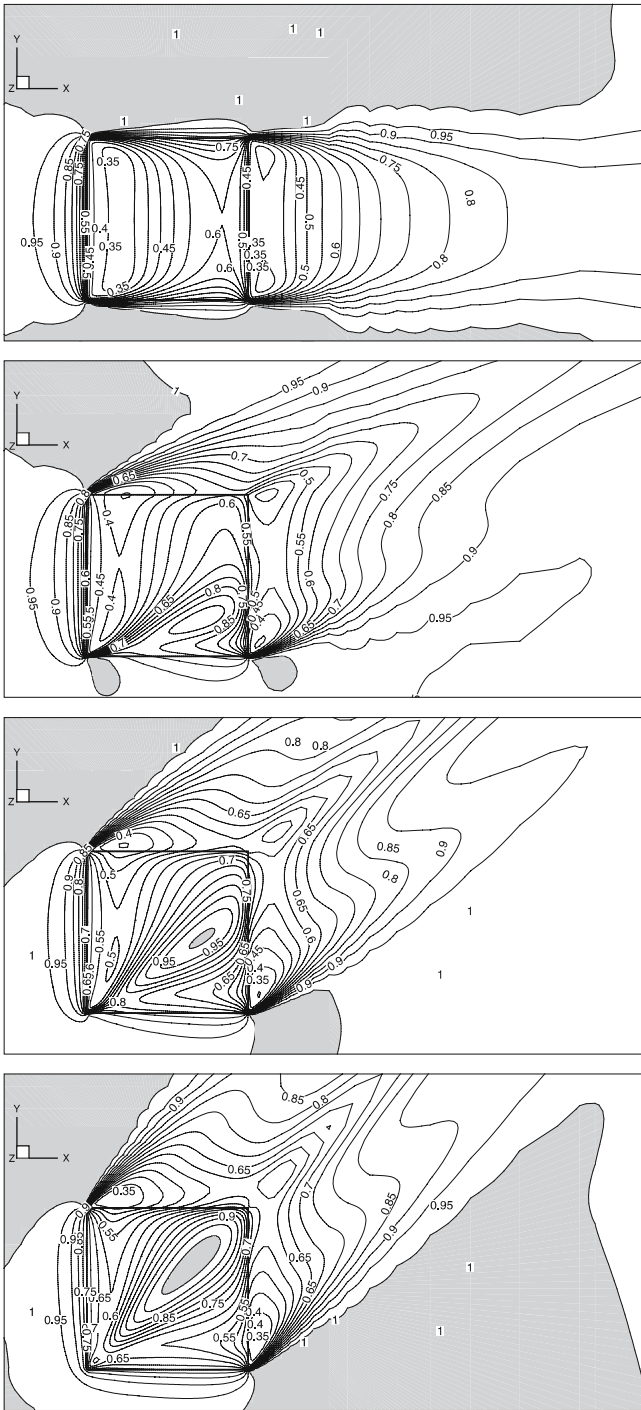


**Fig. 15** Contours of normalized, horizontal wind speed at  $z = h/2$  and around the sheltered square plot; RANS computations, realizable  $k-\epsilon$  closure. The horizontal wind speed,  $S$ , is normalized by its undisturbed value at the same height level,  $S_0$ . In the grey areas,  $S/S_0 \geq 1$ . From top to bottom:  $\beta = \{0^\circ, 15^\circ, 30^\circ, 45^\circ\}$

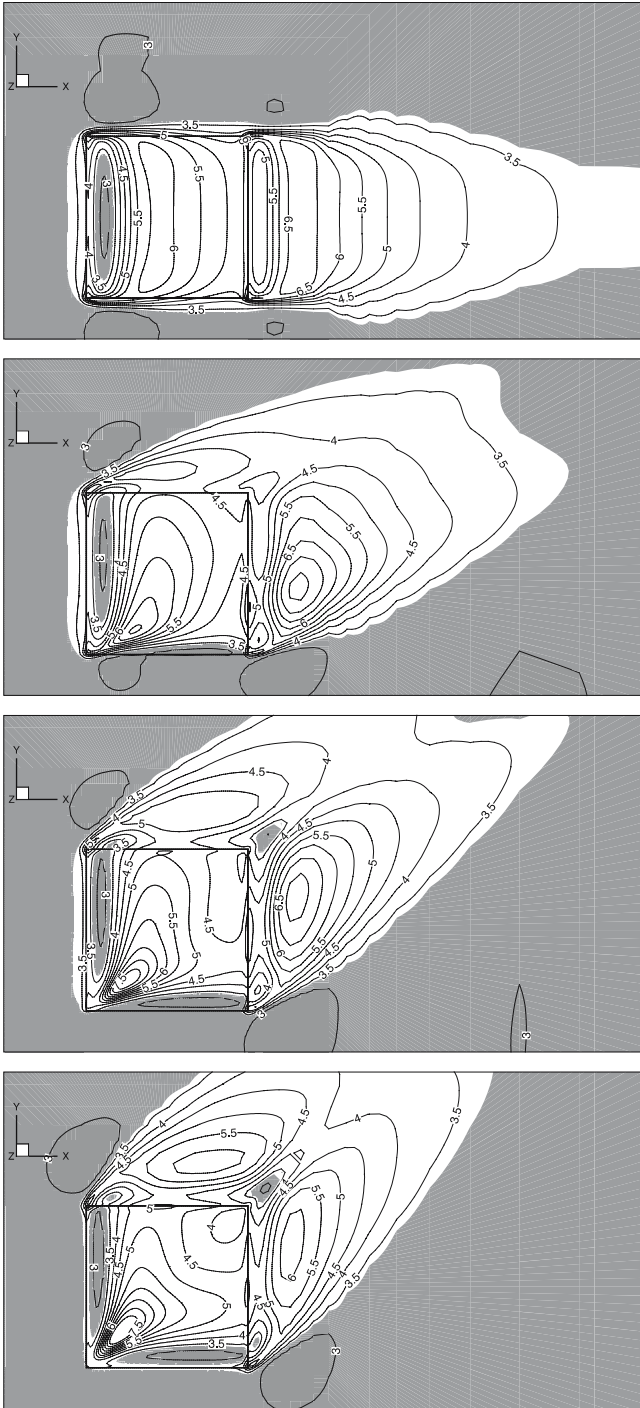


**Fig. 16** Contours of  $\text{TKE}/u_*^2$  (undisturbed value 3.33) at  $z = h/2$  in and around the sheltered square plot; RANS computations, realizable  $k-\epsilon$  closure. From top to bottom:  $\beta = \{0^\circ, 15^\circ, 30^\circ, 45^\circ\}$ . In the grey areas,  $\text{TKE} \leq 3.33u_*^2$

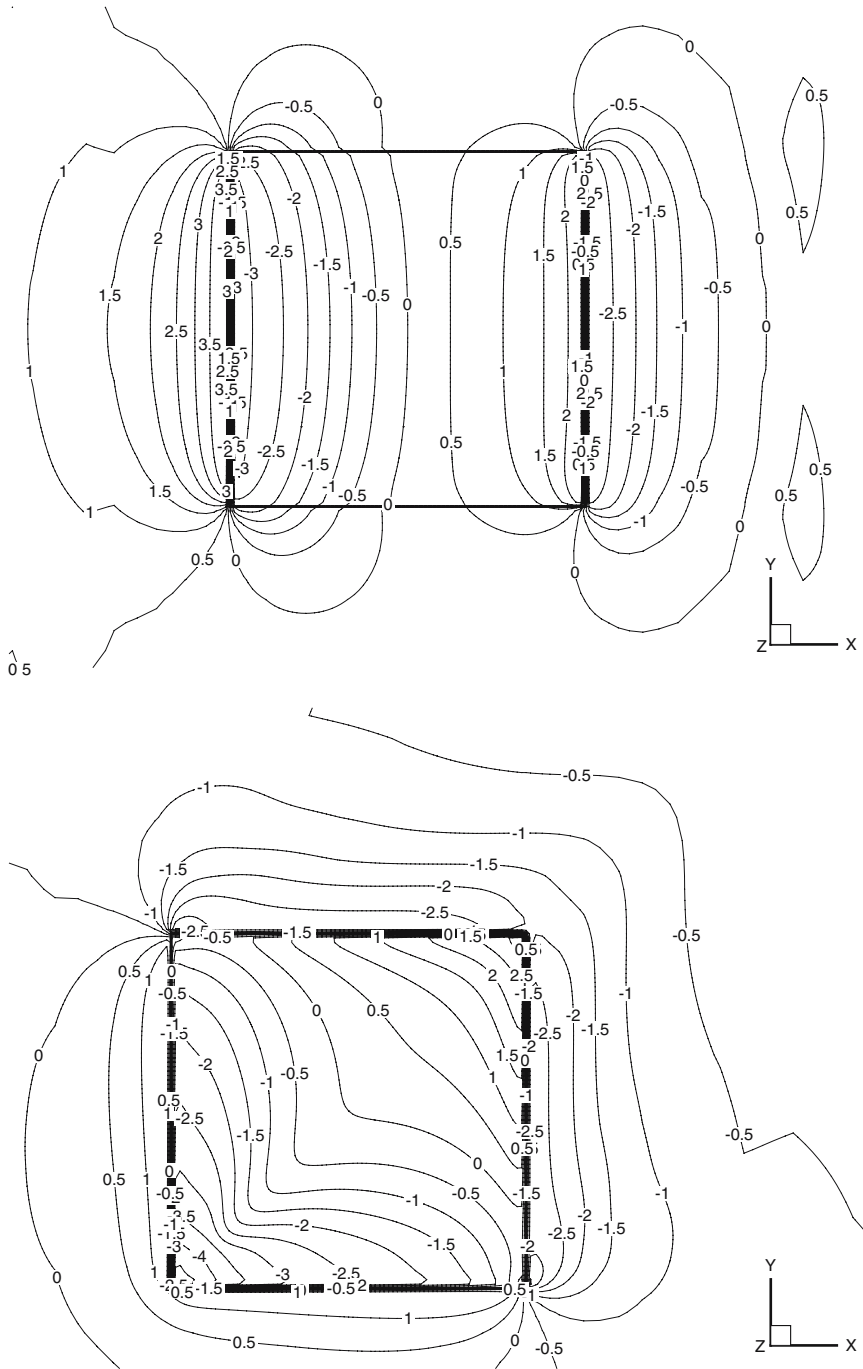


**Fig. 17** Contours of the pressure variation (relative to the pressure value at the square centre, in Pa) at level  $z/h = 0.1$  (RANS computations, realizable  $k - \epsilon$  closure). From top to bottom:  $\beta = \{0^\circ, 45^\circ\}$ . In the normal flow-case ( $\beta = 0^\circ$ ), flow is from left; in the corner-flow case ( $\beta = 45^\circ$ ), flow is from bottom left corner

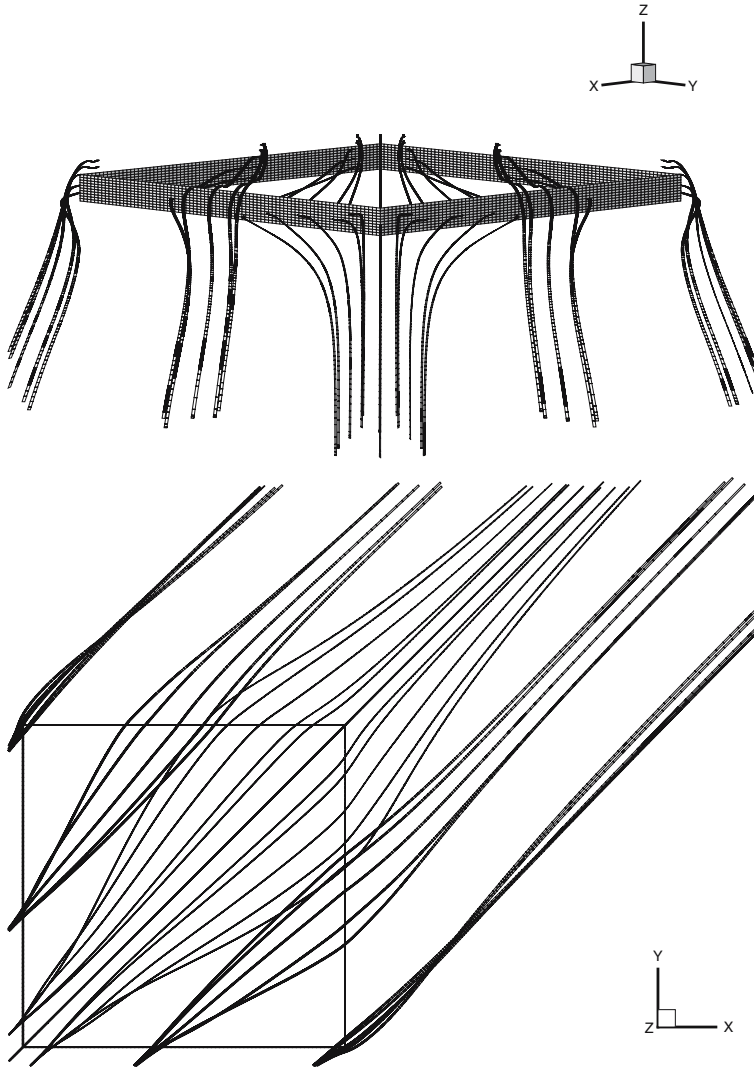


**Fig. 18** Streamlines of the mean flow attacking the square shelterbelt at  $\beta = 45^\circ$  (RANS computations, realizable  $k-\epsilon$  closure). Top: downstream view, flow is towards the bottom of the page; bottom: top view, flow is from bottom left corner

## 5 Conclusions

Relying on experimental data available in the literature, we sought to assess the potential of current CFD methods for predicting disturbed micrometeorological flow, our case in point being that of the porous windbreak standing in an otherwise uniform, neutrally-stratified surface layer. The engineering-standard flow solver, Fluent, was used for the purpose of simulating Reynolds-averaged flows past a long, straight fence (2D simulation) and a square shelterbelt (3D simulation). The 2D simulations were conducted so as to quantify the impact of subjective numerical choices over the numerical solution (such as placement of the com-

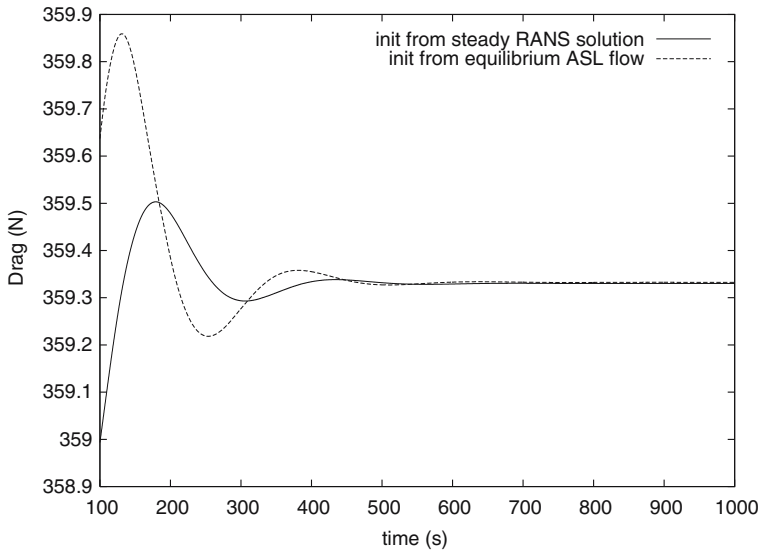


**Fig. 19** Time history of the friction drag acting on the sheltered square area (URANS computations, realizable  $k-\epsilon$  model)

putational domain boundaries, mesh spacing, turbulence closure). As a result, better-practice guidelines for computational windbreak aerodynamics have been drawn up, with a view to making simulation results more objective and less user-dependent: with regard to the interpolation schemes, second-order accuracy should be the bare minimum (as in most engineering applications of CFD). With regard to the grid design, the upstream (inlet) and downstream (outflow) boundaries should be located at least 20 fence heights away from the windbreak, the top boundary should be at least 40 fence heights above the windbreak, the width of the cells adjacent to the windbreak should be less than or equal to  $1/20$  of its height, and the expansion ratio between adjacent cells should not be greater than 1.2. With regard to the turbulence closures, studies conducted on cases where the treatment of the Reynolds stress was the only compromising subjective feature<sup>10</sup> suggested that the so-called “realizable”  $k-\epsilon$  model was the most suitable one (of those offered by Fluent) to fairly reproduce the experimental data. Three-dimensional simulations that followed the above guidelines yielded an agreement with observed mean winds that, though far from perfect, can be said to be much better than simply qualitative. To the question “is CFD reliable for computational windbreak aerodynamics?” our answer is therefore a definite ‘yes’, though only in so far as one’s interest is the mean velocity field, and only provided the CFD user follows relevant guidelines, such as those suggested above.

**Acknowledgements** This work has been supported by research grants from the Natural Sciences and Engineering Research Council of Canada (NSERC) and the Canadian Foundation for Climate and Atmospheric Sciences (CFCAS). The numerical simulations have been enabled by the use of WestGrid computing resources, the latter being funded in part by the Canada Foundation for Innovation, Alberta Innovation and Science, British Columbia Advanced Education, and the participating research institutions. WestGrid equipment is provided by IBM, Hewlett Packard and SGI.

<sup>10</sup> We realize this is a somewhat provocative claim that some may suspect is naive. The sense in which we make it is that we believe we had forced into ‘accuracy-overkill’ all other subjective factors, viz. had attained superfluous resolution, and used high order interpolations.

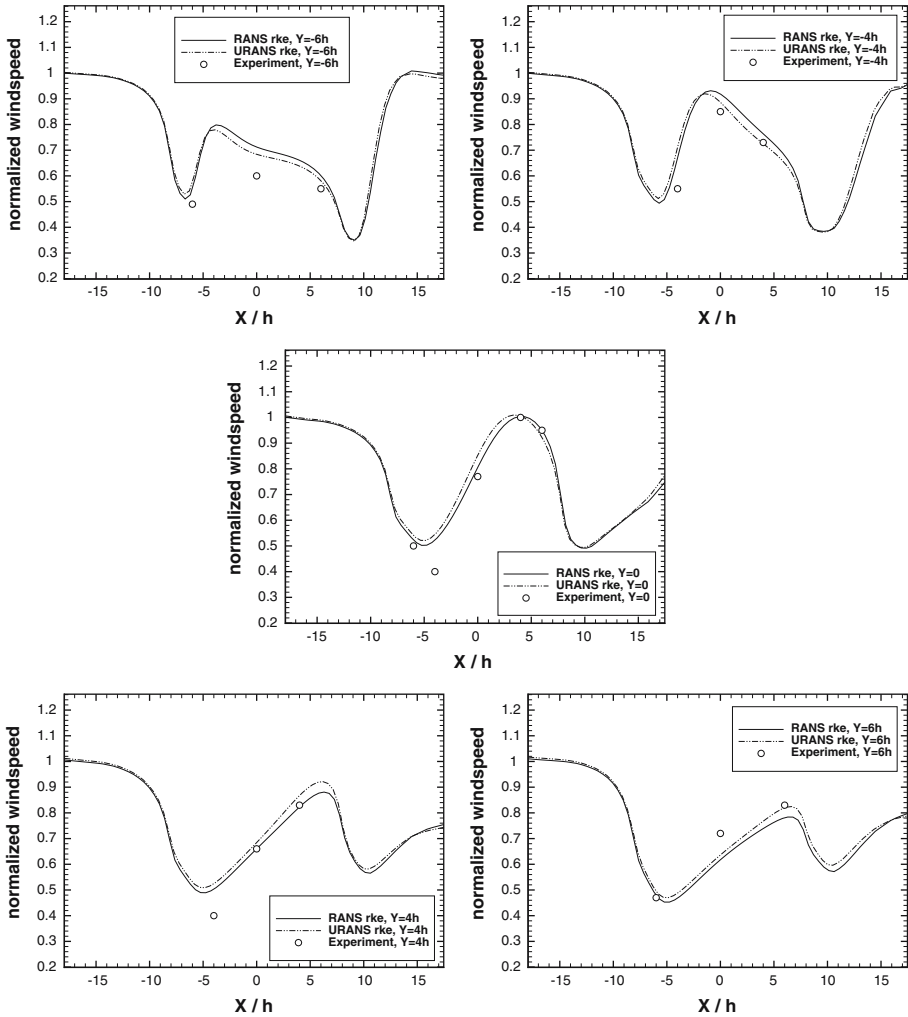


**Fig. 20** Observed and computed (RANS and URANS) horizontal wind speeds at  $z = h/2$  and  $y/h = \{-6, -4, 0, +4, +6\}$  for the square shelterbelt ( $h = 1.25$  m,  $D = 20$  m,  $K_r = 4.8$ ,  $z_0 = 0.015$  m);  $\beta = 30^\circ$ . The wind speed is normalized by its value far upstream at the same height level. Front fence is located at  $x/h = -8$ , rear fence is located at  $x/h = +8$

## Appendix

### A. Details of the Numerical Method

Within each cycle of the iterative solution sequence, the  $x$ ,  $y$ , and  $z$  momentum equations are solved in turn using the values obtained at the end of the previous cycle for the pressure and the cell-face mass flux variables appearing in the convection terms (if the computation has just begun, the prescribed initial values are used instead). Each momentum equation, thus made implicitly linear with respect to its momentum variable, is solved by using a point Gauss–Seidel solver in conjunction with an algebraic multigrid method (AMG) for convergence

acceleration, yielding then an updated velocity field. The face mass fluxes interpolated from these updated velocities are then corrected to satisfy the continuity equation, by solving an equation for the pressure correction (using again Gauss Seidel and AMG), which also allows an update of the pressure field. This pressure-correction technique, based on the SIMPLE family of algorithms (Patankar 1980), postulates that the correction of the normal velocity on a cell face is proportional to the difference between the pressure corrections within the two cells on either side of the face. Once pressure and face mass fluxes are corrected, budget equations for turbulence quantities, if any, are then solved (still sequentially) using the previously updated values of all the other variables. After that, the end of the iteration loop is reached: a check for convergence is made (by computing the global residuals of each equation), and if necessary a new cycle is started. For convergence of the iterative solution procedure, it is necessary to control the change of the dependent variables of interest (momentum, pressure, turbulence quantities). This is done through under-relaxation.

For steady state solutions, the time derivative is not taken into account in the governing equations, thus only the convection, diffusion and source terms contribute to the system of algebraic equations to be solved by the solution procedure outlined above. With regard to the discretization of the convection terms, second-order upwinding was used to interpolate the face value  $\phi_f$  of the ‘convected’ dependent variable  $\phi$ :

$$\phi_f = \phi + \vec{\nabla}\phi \cdot \vec{\delta}s, \quad (12)$$

where  $\phi$  and  $\vec{\nabla}\phi$  are the cell-centred value of the dependent variable of interest and its gradient in the upstream cell, and  $\vec{\delta}s$  is the displacement vector from the upstream cell centroid to the face centroid. The gradient within the upstream cell is computed using the divergence (Green–Ostrogradsky) theorem, which in discrete form yields:

$$\vec{\nabla}\phi = \frac{1}{V} \sum_f \tilde{\phi}_f \vec{A}, \quad (13)$$

where  $\vec{A}$  is the face area vector,  $V$  is the volume of the computational cell, and  $\tilde{\phi}_f$  is the face value computed by averaging  $\phi$  from the two cells adjacent to the face. For the diffusion terms (turbulent or molecular), central schemes were used: the requested face values of the gradients were obtained through the arithmetic averaging of the gradient values at the two neighbouring cell centres (the gradient within one cell being computed from Eq. 13).

When the unsteady form of the governing equations was solved, second-order accuracy in time was obtained using the following implicit scheme:

$$\phi^{n+1} = 4/3\phi^n - 1/3\phi^{n-1} + 2/3\Delta t F(\phi^{n+1}), \quad (14)$$

where superscript  $n$  refers to the current time level,  $\phi$  to the dependent variable of interest, and  $F(\phi)$  to a function incorporating the previously-described spatial discretizations (convection and diffusion terms). The iterative solution procedure outlined earlier is used to solve for  $\phi^{n+1}$  at the cell centres. To cover the desired time period of the transient simulation, the whole process has to be repeated several times (every converged execution of the iterative solution procedure advancing the solution from the current time level to the next one).

## B. RANS Output Compared to Measurements from Cup Anemometers

We discuss here which model output (or function of model outputs) is most properly comparable with the wind statistic measured in the windbreak flows, namely mean cup wind speed  $S = \sqrt{u^2 + v^2}$ .

Provided the magnitudes of the velocity fluctuations  $u'$ ,  $v'$  are small relative to mean velocity, mean cup wind speed can be related to the mean and standard deviation of the horizontal velocity components by

$$S = Q \left( 1 + \frac{\overline{u'^2} + \overline{v'^2}}{2Q^2} \right), \quad (15)$$

where  $Q^2 = \bar{u}^2 + \bar{v}^2$ . Focusing on the measurements at Ellerslie (e.g. square plot, measurement height  $z = 0.63$  m, roughness length  $z_0 = 0.015$  m), as noted by Wilson (2004a, p. 1164) in equilibrium surface-layer flow, typical magnitudes of the  $u'$ ,  $v'$  fluctuations relative to mean cup wind speed  $S$  are

$$\frac{\sigma_u}{S} \approx \frac{\sigma_v}{S} \approx \frac{0.8}{\ln(z/z_0)} \approx 0.2, \quad (16)$$

so that the measured transects should predominantly reflect changes in mean wind speed. Because RANS models are known to give poorer predictions of turbulence statistics than of mean wind, we simply estimated 'RANS-predicted cup wind speed' as  $S_{\text{RANS}} = Q = \sqrt{\bar{u}^2 + \bar{v}^2}$ .

## References

- Bradley EF, Mulhearn PJ (1983) Development of velocity and shear stress distributions in the wake of a porous shelter fence. *J Wind Eng Ind Aerodyn* 15:145–156
- Lauder BE (1989) Second-moment closure and its use in modeling turbulent industrial flows. *Int J Numer Methods Fluids* 9:963–985
- Lauder BE, Spalding DB (1972) Lectures in mathematical models of turbulence. Academic Press, London, England, pp 90–110
- Lien FS, Leschziner MA (1994) Assessment of turbulent transport models including non-linear RNG eddy-viscosity formulation and second-moment closure. *Comput Fluids*, 23(8):983–1004
- Lien FS, Yee E, Wilson JD (2005) Numerical modelling of the turbulent flow developing within and over a 3-D building array, Part II: a mathematical foundation for a distributed drag force approach. *Boundary-Layer Meteorol* 114:245–285
- Packwood AR (2000) Flow through porous fences in thick boundary layers: comparisons between laboratory and numerical experiments. *J Wind Eng Ind Aerodyn* 88:75–90
- Patankar SV (1980) Numerical heat transfer and fluid flow. McGraw-Hill
- Shih T-H, Liou WW, Shabbir A, Yang Z, Zhu J (1995) A new  $k-\epsilon$  eddy-viscosity model for high Reynolds number turbulent flows—model development and validation. *Comput Fluids*, 24(3):227–238
- Speziale CG, Sarkar S, Gatski TB (1991) Modelling the pressure–strain correlation of turbulence: an invariant dynamical systems approach. *J Fluid Mech* 227:245–272
- van Doormaal JP, Raithby GD (1984) Enhancements of the SIMPLE method for predicting incompressible fluid flows. *Numer Heat Transfer* 7:147–163
- Wang H, Takle ES (1995) A numerical simulation of boundary-layer flows near shelterbelt. *Boundary-Layer Meteorol* 75:141–173
- Wilson JD (1985) Numerical studies of flow through a windbreak. *J Wind Eng Ind Aerodyn* 21:119–154
- Wilson JD (2004a) Oblique, stratified winds about a shelter fence I: measurements. *J Appl Meteorol* 43:1149–1167
- Wilson JD (2004b) Oblique, stratified winds about a shelter fence II: comparison of measurements with numerical models. *J Appl Meteorol* 43:1392–1409
- Wilson JD, Flesch TK (2003) Wind measurements in a square plot enclosed by a shelter fence. *Boundary-Layer Meteorol* 109:191–224
- Wilson JD, Yee E (2003) Calculation of winds disturbed by an array of fences. *Agric For Meteorol* 115:31–50
- Yakhot V, Orszag SA (1986) Renormalization group analysis of turbulence: I. Basic theory. *J Sci Comput* 1(1):1–51